Science Advances
AAAS

advances.sciencemag.org/cgi/content/full/3/4/e1602570/DC1

Supplementary Materials for

Toward continuous-wave operation of organic semiconductor lasers

Atula S. D. Sandanayaka, Toshinori Matsushima, Fatima Bencheikh, Kou Yoshida, Munetomo Inoue, Takashi Fujihara, Kenichi Goushi, Jean-Charles Ribierre, Chihaya Adachi

Published 28 April 2017, *Sci. Adv.* **3**, e1602570 (2017)
DOI: 10.1126/sciadv.1602570

This PDF file includes:

- section S1. Optical simulations
- section S2. Lasing properties of mixed-order DFB devices
- section S3. Optical gain
- section S4. Transient absorption
- section S5. Thermal simulations
- fig. S1. Schematic of the geometry used for optical simulation.
- fig. S2. Lasing threshold of mixed-order DFB lasers based on BSBCz:CBP (6:94 wt %) 200-nm-thick film for different dimensions of the second-order gratings.
- fig. S3. Photophysical properties of films with and without encapsulation.
- fig. S4. Characterization of the pulsed organic lasers.
- fig. S5. qCW lasing threshold.
- fig. S6. Lasing threshold measured in forward (increasing repetition rate) and reverse (decreasing repetition rate) directions as a function of the repetition rate.
- fig. S7. Significant reduction of degradation in encapsulated DFB devices.
- fig. S8. Stability of the qCW laser.
- fig. S9. Optical net gain under long-pulse operation.
- fig. S10. Emission spectra of encapsulated 20 wt % blend mixed-order DFB lasers measured at a pumping intensity of 200 W cm^{-2} and 2.0 kW cm^{-2} for long-pulse durations of 800 μs and 30 ms, respectively.
- fig. S11. Streak camera image showing laser emission integrated over 100 pulses from an encapsulated mixed-order DFB device during a 30-ms-long photoexcitation with a pump power of 2.0 kW cm^{-2}.
- fig. S12. Lack of triplet losses in the gain medium.
- fig. S13. Divergence of DFB laser.
- fig. S14. Polarization of DFB laser.

- fig. S15. Lasing threshold under long-pulse operation.
- fig. S16. Excitation duration dependence of the lasing threshold.
- fig. S17. Laser-induced thermal degradation.
- fig. S18. Schematic of the geometry used for thermal simulation.
- fig. S19. Maximum temperature rise at the end of each pulse.
- fig. S20. Temperature rise as a function of time with different pulse widths.
- fig. S21. Temperature rise as a function of time for a pulse width of 10 ms in the devices with and without encapsulation.
- fig. S22. Temperature rise as a function of time or number of pulses of τ_p = 30 ms in the gain region.
- table S1. Film thickness, lasing wavelength, confinement factor, and quality factor.
- table S2. Grating depth, lasing wavelength, confinement factor, and quality factor.
- table S3. Comparison between devices with and without encapsulation, lasing wavelength, confinement factor, and quality factor.
- table S4. Pulse width, excitation power, net gains, and loss coefficient.
- table S5. Thermophysical and geometrical parameters of the materials.
- References (*50*–*52*)

section S1. Optical simulations

The confinement factor (Γ) and the quality factor (Q-factor) are calculated to design the resonant cavity. These two factors are extracted from the calculation of the eigenvalues of resonant cavity mode by solving Maxwell's equation using the finite element method in the Radio Frequency module of COMSOL 5.2a software. The computation domain is limited to one-unit domain (see fig. S1) consisting of a second-order grating enclosed by two first-order gratings. The Floquet periodic boundary conditions are applied for lateral boundaries and scattering boundary conditions are used for the top and bottom boundaries. Then, the eigenvalues of the resonant cavity eigenmodes are calculated. From the real and imaginary parts of the eigenvalue, the Q-factor, is derived using $Q=\omega_0 / (2|\alpha|)$ where ω_0 is the resonance angular frequency and α is the damping coefficient ($|\alpha|=1/\tau$).

The input parameters used for the optical simulation are the organic film thickness and the refractive indices of the layers. The CYTOP (n_{CYTOP}=1.35) and the SiO_2 substrate (n_{SiO2}=1.46) are considered to be semi-infinite layers. The refractive index of the 6wt% BSBCz:CBP film, n_f, is considered to be equal to the reported refractive index of CBP (n_f=1.85) (*50*). The thickness d_0 of the BSBCz:CBP film is changed from 100 to 300 nm. Due to the top surface structuration, a thin grating is added with a depth $h_{g(top)}$ = 5 nm on a thin layer of thickness $(h_g-h_{g(Top)})/2$ = 30 nm.

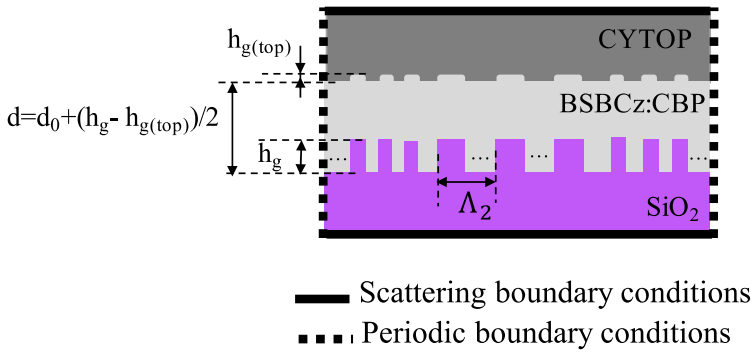

fig. S1. Schematic of the geometry used for optical simulation.

1.1 Film thickness variation

First, we investigate the effect of variation of the film thickness d_0 while keeping the grating depth h_g constant (h_g=65 nm) by calculating the Γ and the Q-factor. Table S1 shows the calculation results.

table S1. Film thickness, lasing wavelength, confinement factor, and quality factor.

d_0 (nm)	λ_0 (nm)	Q-factor	Γ
100	465	717	0.34
200	481	5050	0.78
300	494	6674	0.88

When the thickness increases, the Γ and the Q-factor increase but, due to the shift of the resonant wavelength λ_0 from the ASE wavelength of the gain material, a d_0 of 200 nm remains an optimal thickness for the device operation.

1.2 Grating depth variation

Second, we investigate the effect of h_g variation while keeping d_0 constant (d=200 nm) by calculating the Γ and the Q-factor. Table S2 below shows the calculation results.

table S2. Grating depth, lasing wavelength, confinement factor, and quality factor.

h_g (nm)	λ_0 (nm)	Q-factor	Γ
30	481	8026	0.79
65	481	5050	0.78
80	483	1915	0.74

By reducing the grating depth, the Q-factor increases while Γ remains almost the same. However, fabrication of a shallow grating is challenging since a small variation of the depth would dramatically affect the optical response of the grating. While this aspect can certainly be improved in future works, the choice of the 65 nm depth in this study seems to be the most appropriate.

1.3 Comparison between devices with and without encapsulation

The calculation is done using the same geometry. With encapsulation, the top layer is the CYTOP with a refractive index of 1.35. Without encapsulation, the CYTOP is replaced by air (n=1). In this case the Q-factor and Γ increase and the resonant wavelength is slightly blue shifted, as shown in table S3.

table S3. Comparison between devices with and without encapsulation, lasing wavelength, confinement factor, and quality factor.

	λ_0 (nm)	Q-factor	Γ
With encapsulation	481.2	5050	0.78
Without encapsulation	479	6455	0.82

However, based on the experimental results, the device with encapsulation showed better performance (FWHM) than the one without encapsulation. This can be due to changes of top surface when we encapsulated the device or due the protection from moisture.

1.4 Influence of the dimension of the 2nd order grating regions

The lasing thresholds of BSBCz:CBP (6:94 wt.%) blend mixed-order DFB lasers were determined experimentally using different dimensions for the 2nd order regions. The results are displayed in fig. S2. It can be seen that the DFB architecture used in this study (which corresponds to a number of periods equal to 36) is not fully optimized, suggesting that further improvements of the device performances should be possible by simply playing on the resonator structure.

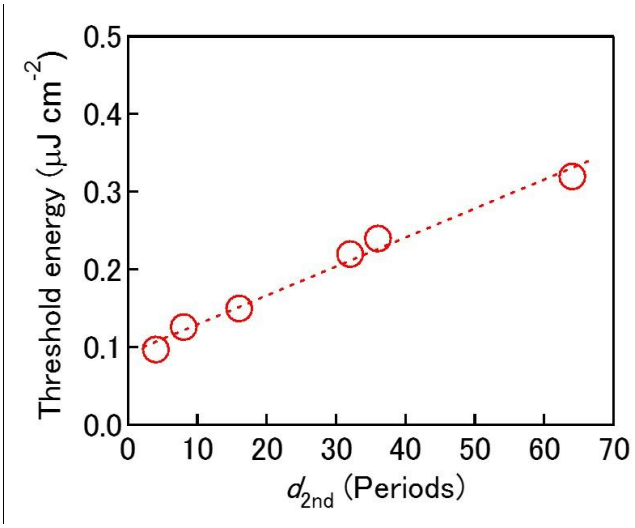

fig. S2. Lasing threshold of mixed-order DFB lasers based on BSBCz:CBP (6:94 wt %) 200-nm-thick film for different dimensions of the second-order gratings. The devices were optically pumped by nitrogen laser delivering 800 ps pulses at a repetition rate of 20 Hz and a wavelength of 337 nm.

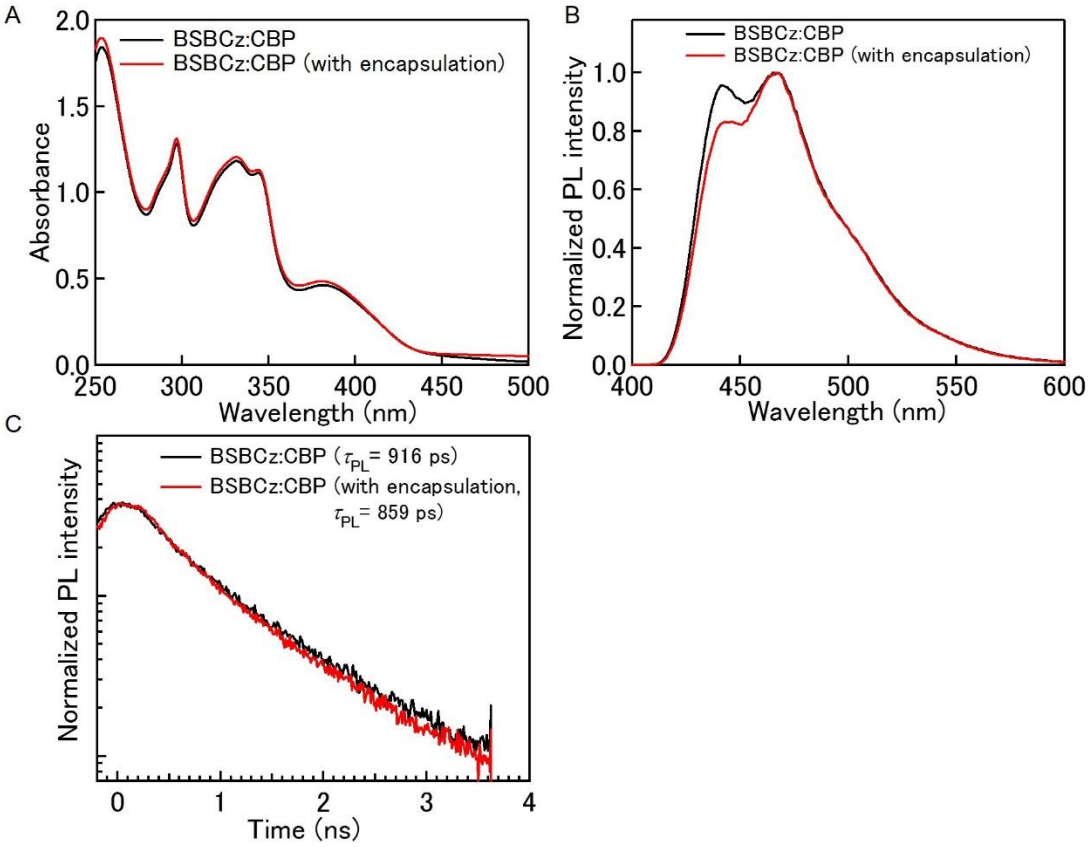

fig. S3. Photophysical properties of films with and without encapsulation. (**A**) Absorption spectra, (**B**) steady-state photoluminescence spectra and (**C**) transient photoluminescence decays of BSBCz:CBP (6:94 wt.%) films with and without encapsulation by a CYTOP film.

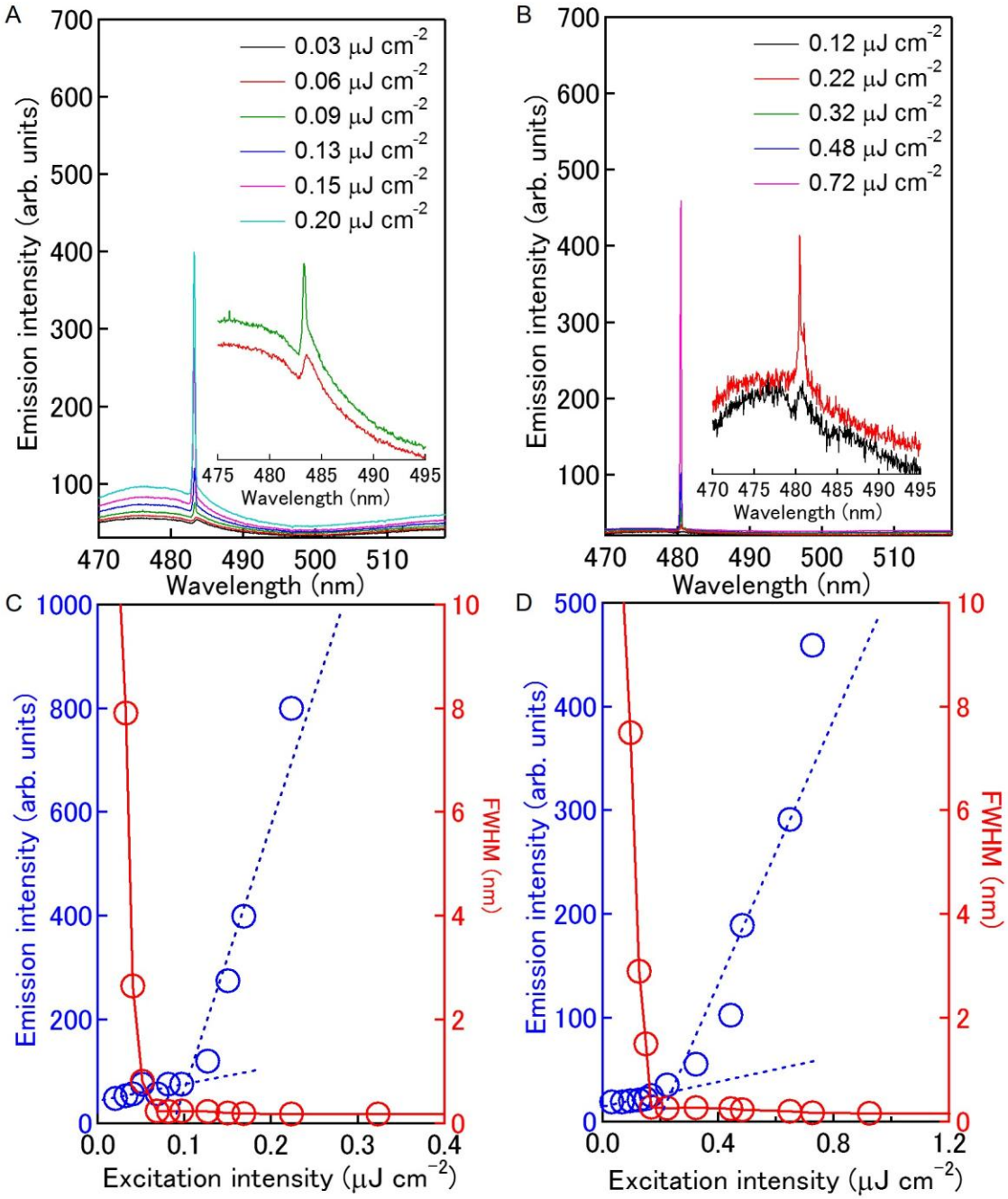

fig. S4. Characterization of the pulsed organic lasers. Emission spectra of representative organic mixed-order DFB lasers based on (**A**) BSBCz:CBP (6:94 wt.%) and (**B**) BSBCz neat films at various pumping intensities below and above the lasing threshold. The insets show the emission spectra near the lasing threshold. Emission output intensity and FWHM as a function of the pumping intensity in the (**C**) blend and (**D**) neat film DFB lasers. In these experiments, the organic films were covered by spin-coated CYTOP films and a sapphire lid. The optical pumping source was a nitrogen laser emitting 0.8-ns-wide pulse excitation at a repetition rate of

20 Hz and a wavelength of 337 nm. The emission from the laser devices was collected in the direction normal to the substrate plane.

section S2. Lasing properties of mixed-order DFB devices

The lasing properties of encapsulated mixed-order DFB devices using either a BSBCz neat film or a BSBCz:CBP (6:94 wt.%) blend film as the gain medium were examined under pulsed optical pumping using a nitrogen laser delivering 800 ps pulses at a repetition rate of 20 Hz and at a wavelength of 337 nm. In case of the CBP blend films, the excitation light was mainly absorbed by the CBP host. However, the large spectral overlap between CBP emission and BSBCz absorption guaranteed an efficient Förster-type energy transfer from the host to the guest molecules (*35*-*39*). This was confirmed by the absence of CBP emission under 337 nm photo-excitation. Figures S4A-B display the emission spectra collected normal to the surface of the BSBCz and BSBCz:CBP (6:94 wt.%) films at different excitation intensities below and above the threshold. At low excitation intensities, Bragg dips corresponding to the optical stopband of the DFB grating (*35*) were observed at 480 and 483 nm for the neat and blend films, respectively. The tiny variation in the Bragg dip position is presumably due to the slightly different refractive indices of the blend and neat films (*35*-*39*). As the pumping intensity was increased above a critical threshold, a narrow emission peak appeared in both neat and blend devices, indicating the onset of lasing. It can also be seen that the laser peaks increased in intensity faster than the photoluminescence backgrounds providing evidence of the non-linearity associated with stimulated emission. The lasing wavelength was found to be 484 nm for the blend film and 481 nm for the neat film. Figures S4C-D show the output emission intensity and the full-width-at-half-maximum (FWHM) as a function of the pumping intensity for both DFB devices. The FWHM was found to become lower than 0.2 nm at high excitation intensities. The lasing thresholds of the DFB lasers were determined from the abrupt changes in the output intensities. The devices based on neat and blend films were found to exhibit lasing thresholds of 0.22 and 0.09 $\mu J\ cm^{-2}$, respectively. In both cases, these values are lower than the previously reported thresholds for amplified spontaneous emission (ASE) and the second-order DFB lasers in BSBCz:CBP blends (*35*-*39*), supporting the potential of mixed-order gratings for high performance organic solid-state lasers.

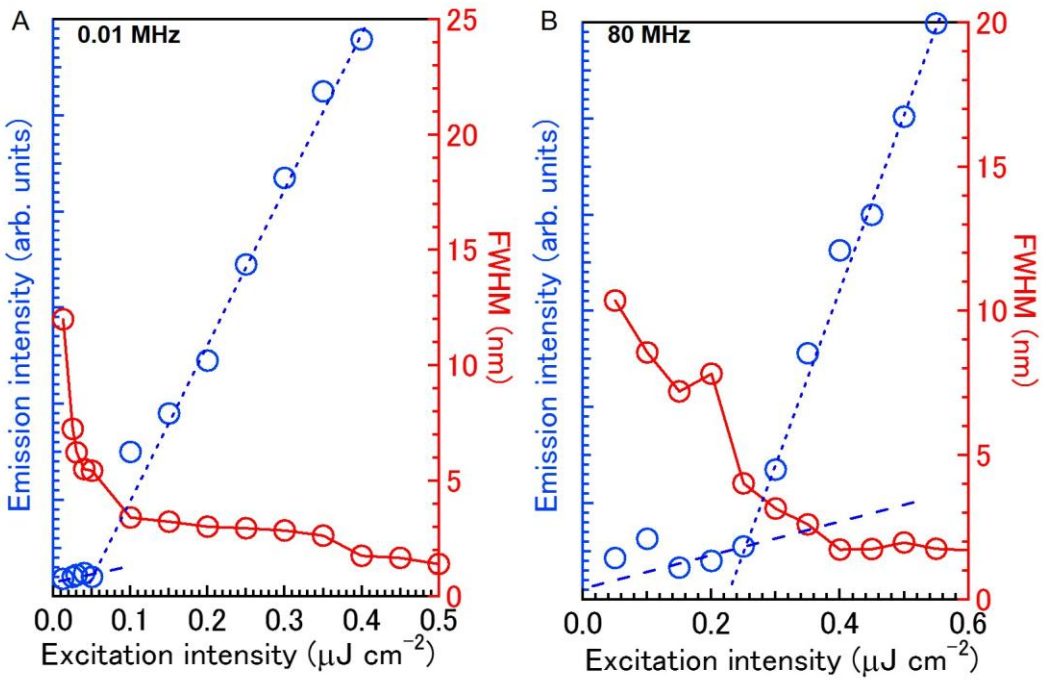

fig. S5. qCW lasing threshold. Emission output intensity and FWHM as a function of the pumping intensity in a representative encapsulated blend mixed-order DFB laser at a repetition rate of (**A**) 0.01 MHz and (**B**) 80 MHz.

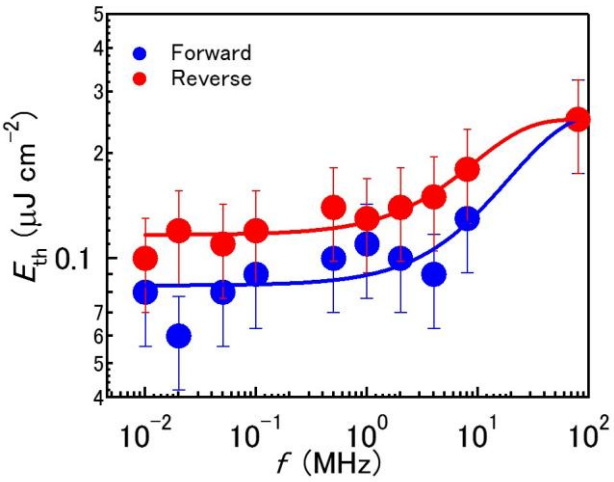

fig. S6. Lasing threshold measured in forward (increasing repetition rate) and reverse (decreasing repetition rate) directions as a function of the repetition rate. The irreversible changes in lasing threshold are attributed to a degradation of the gain medium under intense photo-excitation.

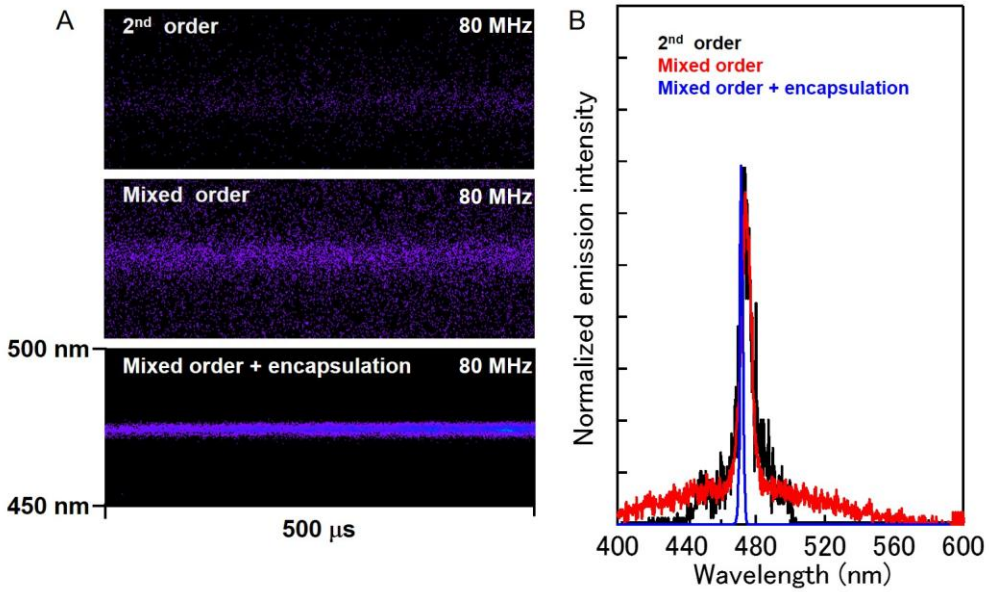

fig. S7. Significant reduction of degradation in encapsulated DFB devices. (**A**) Streak camera images and (**B**) corresponding emission spectra showing the emission from a non-encapsulated 2nd order, a non-encapsulated mixed-order and an encapsulated mixed-order DFB device at a repetition rate of 80 MHz and a pumping intensity of 0.5 μJ cm^{-2}.

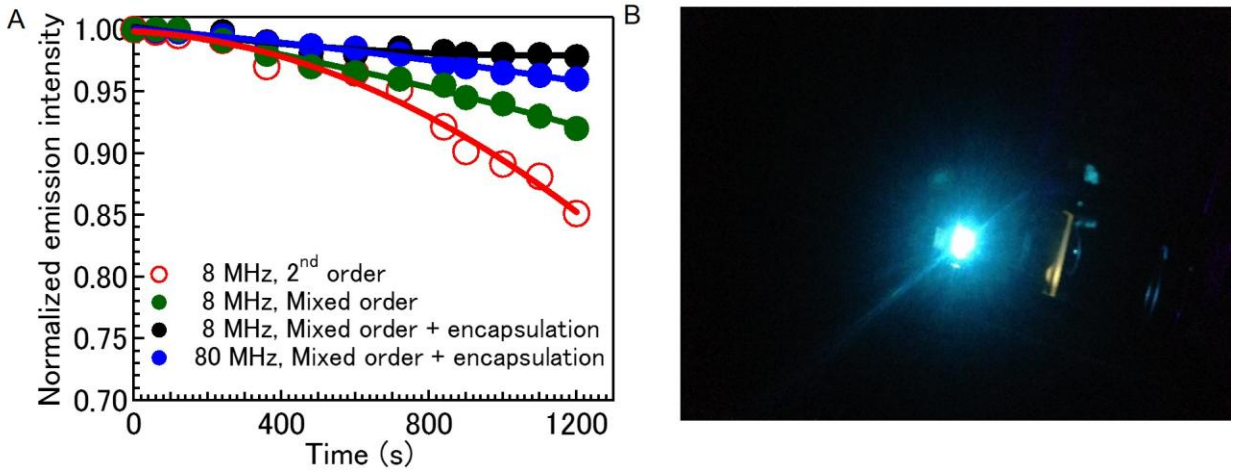

fig. S8. Stability of the qCW laser. (**A**) Operational stability of the laser output oscillations from different organic DFB lasers based on BSBCz:CBP (6:94 wt.%) blend films. To measure the stability, the laser devices were continuously quasi-CW operated at 8 MHz or 80 MHz for 20 minutes. For each device, the excitation light intensity was 1.5 times that of its lasing threshold. (**B**) Photograph of the encapsulated blend DFB laser operating in the quasi-CW regime at 80 MHz.

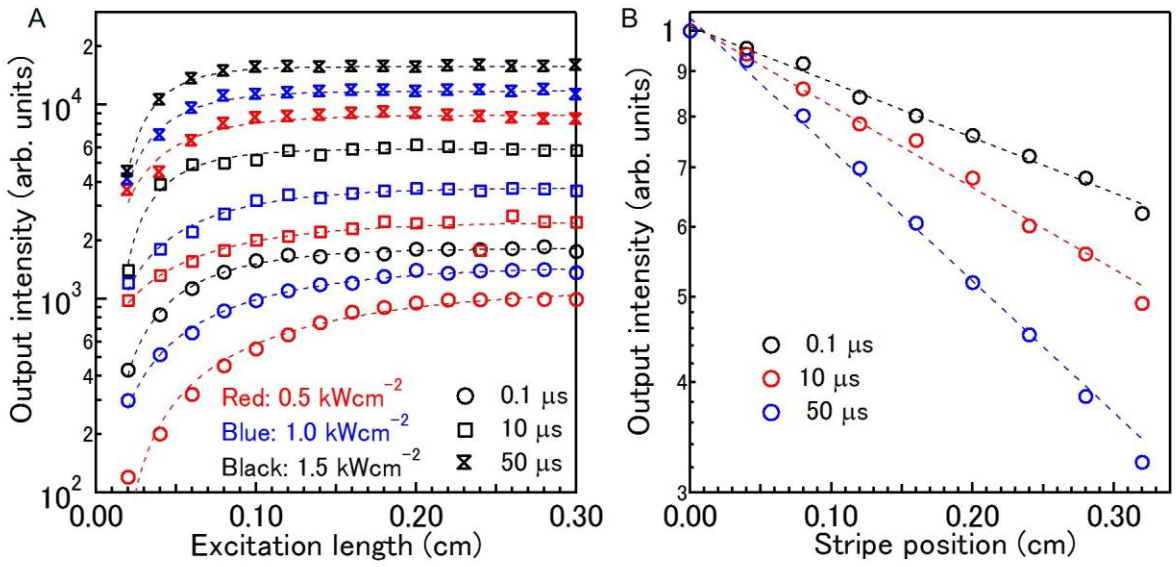

fig. S9. Optical net gain under long-pulse operation. (**A**) Output intensity of the ASE centered at 472 nm as a function of the pump energy and the stripe length in a 200-nm-thick BSBCz:CBP (20:80 wt.%) film. The dash lines are fits to the data using equations reported in references (*7*, *11*). The net gain of the waveguide was determined from the fits. (**B**) ASE intensity emitted from the edge of the waveguide film versus the distance between the pump stripe and the edge of the blend film. The ASE characteristics of the film were investigated using an inorganic laser diode emitting at 405 nm with different (0.1, 10 and 50 μs) pulse widths.

section S3. Optical gain

From these experimental ASE data, the net gain and loss coefficients could be determined and their values are listed in table S4.

table S4. Pulse width, excitation power, net gains, and loss coefficient.

Pulse width (μs)	Power (k W cm^{-2})	Net gains (cm^{-1})	Loss coefficient (cm^{-1})
0.1	0.5	8.1	1.5
	1.0	11.3	
	1.5	19.8	
10.0	0.5	13.9	2.2
	1.0	17.0	
	1.5	32.6	
50.0	0.5	25.1	3.4
	1.0	30.8	
	1.5	40.1	

These ASE results provide clear evidence that a large net optical gain can be achieved in BSBCz based films in the CW regime. Therefore, this clearly supports our statement that BSBCz is one of the best candidates for CW and quasi-CW lasing.

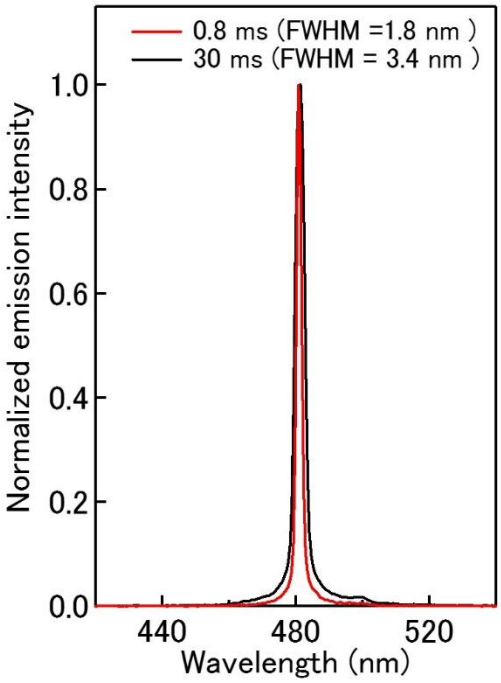

fig. S10. Emission spectra of encapsulated 20 wt % blend mixed-order DFB lasers measured at a pumping intensity of 200 W cm^{-2} and 2.0 kW cm^{-2} for long-pulse durations of 800 μs and 30 ms, respectively.

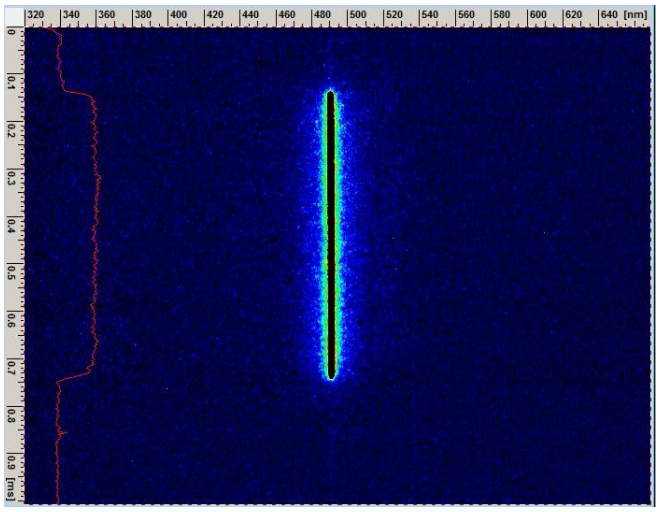

fig. S11. Streak camera image showing laser emission integrated over 100 pulses from an encapsulated mixed-order DFB device during a 30-ms-long photoexcitation with a pump power of 2.0 kW cm^{-2}. The gain medium was a BSBCz:CBP (20:80 wt.%). Excitation wavelength was 405 nm. To observe lasing during 30 ms with our streak camera system, the duty cycle percentage was changed into 2% to visualize the 30 ms pulse in a 1 ms frame (0.02 × 30 ms = 0.6 ms).

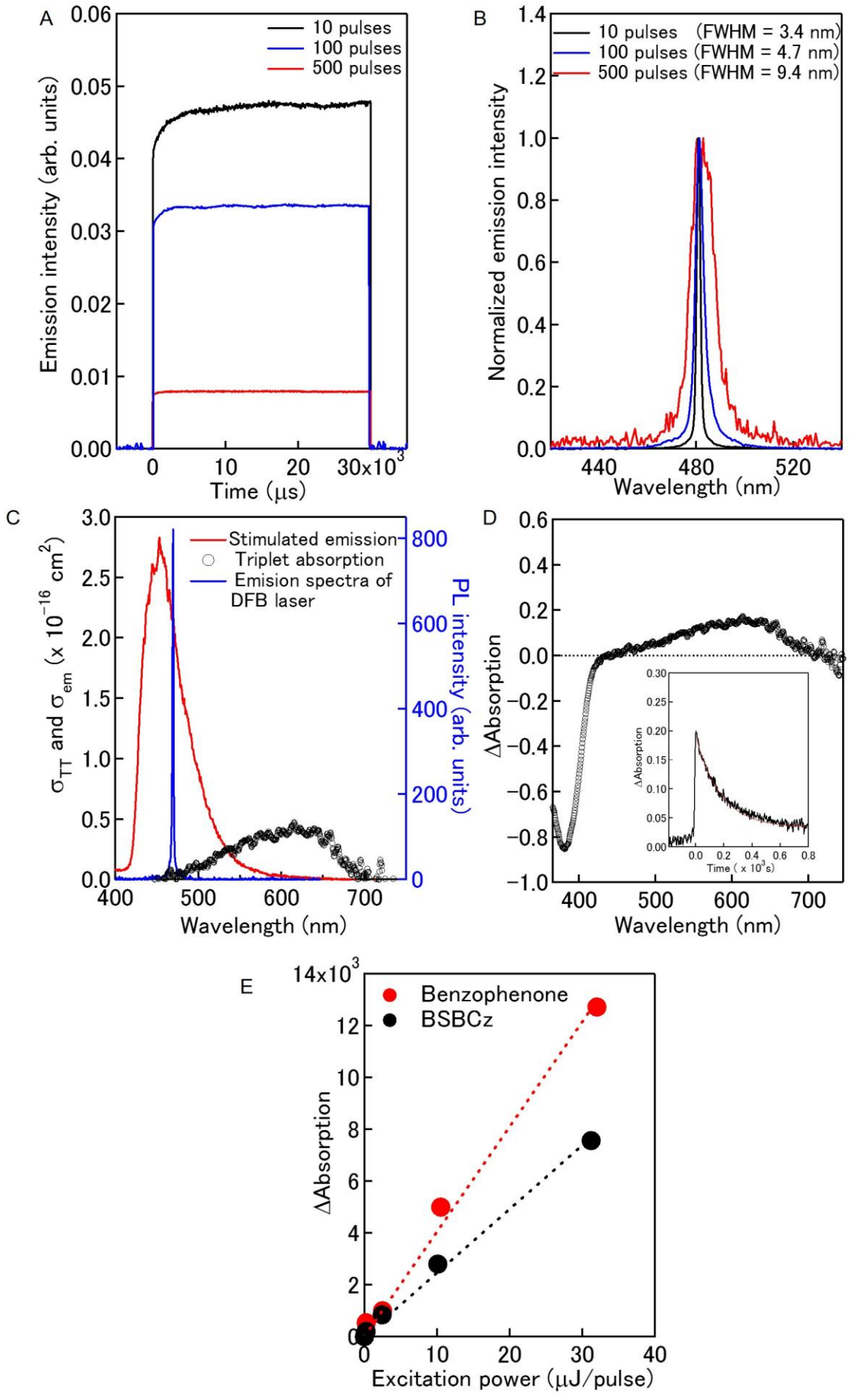
A
Emission intensity (arb. units)
Time (μs)
10 pulses
100 pulses
500 pulses
B
Normalized emission intensity
Wavelength (nm)
10 pulses (FWHM = 3.4 nm)
100 pulses (FWHM = 4.7 nm)
500 pulses (FWHM = 9.4 nm)
C
σTT and σem (x 10−16 cm2)
PL intensity (arb. units)
Wavelength (nm)
Stimulated emission
Triplet absorption
Emision spectra of DFB laser
D
ΔAbsorption
Wavelength (nm)
Time (x 10^3 s)
E
ΔAbsorption
Excitation power (μJ/pulse)
Benzophenone
BSBCz

fig. S12. Lack of triplet losses in the gain medium. (**A**) Temporal evolution of the lasing output intensity, (**B**) emission spectra of the encapsulated mixed-order DFB laser measured after 10 and 500 average pulses with width of 30 ms and pumping intensities of 2.0 kW cm^{-2}. (**C**) Stimulated emission and triplet absorption cross section spectra of BSBCz. Emission spectra of DFB laser were measured from the BSBCz neat film above E_{th}. (**D**) Triplet absorption spectra were measured in a solution containing BSBCz under Ar. (**E**) Excitation power dependence of transient absorption spectra in solution (BSBCz in dichloromethane and benzophenone in benzene).

section S4. Transient absorption

The results in fig. S12A indicate that the PL intensity remains constant after a few μs irradiation. This implies that there is no quenching of the singlet excitons by STA in the devices. Figure S12C also shows that there is no significant spectral overlap between the lasing and the triplet absorption spectra. Those results provide clear evidence that there are no detrimental triplet losses in the gain medium used in this study.

From these data, we also estimated the stimulated emission cross section σ_{em} and the triplet excited state cross sections σ_{TT} as previously report (*36, 51*). The σ_{em} at 480 nm is 2.2 x 10^{-16} cm^2, which is significantly larger than a σ_{TT} of 3.0 x 10^{-19} cm^2, indicating that the triplet absorption has almost no influence on the long pulse regime.

We estimated triplet lifetime (τ_{TT}), triplet absorption cross section (σ_{TT}), and intersystem crossing yield (ϕ_{ISC}) τ_{TT}=5.7 x 10^3 s^{-1}, σ_{TT}=3.89 x 10^{-17} cm^2 (at 630 nm, fig. S12D) and ϕ_{ISC}=0.04, respectively, in a solution. The ϕ_{ISC} was estimated by excitation power dependence of transient absorption (fig. S12E) comparing with benzophenone as a reference (*51*). However, it should be highlighted that we could not observe any triplet contribution in thin films using our transient absorption measurement system. For instance, the intersystem crossing in the blend films is negligible due to the Φ_{PL} value of nearly 100%.

Overall, the emission spectrum measured above E_{th} does not largely overlap with the triplet absorption spectrum, leading to a large net gain for light amplification in the long pulse regime.

Therefore, we are convinced that BSBCz is one of the best candidates for CW and quasi-CW lasing.

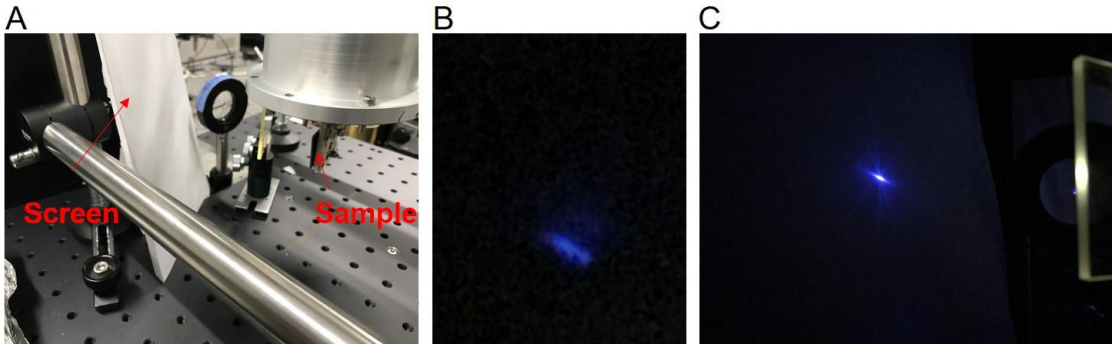

fig. S13. Divergence of DFB laser. (**A**) Pictures showing the divergence of the emitted beam of a DFB laser (**B**) near and (**C**) above the threshold. The active gain medium was a BSBCz:CBP (20:80 wt.%) film. The device was pumped by long pulse regime (10 ms excitation).

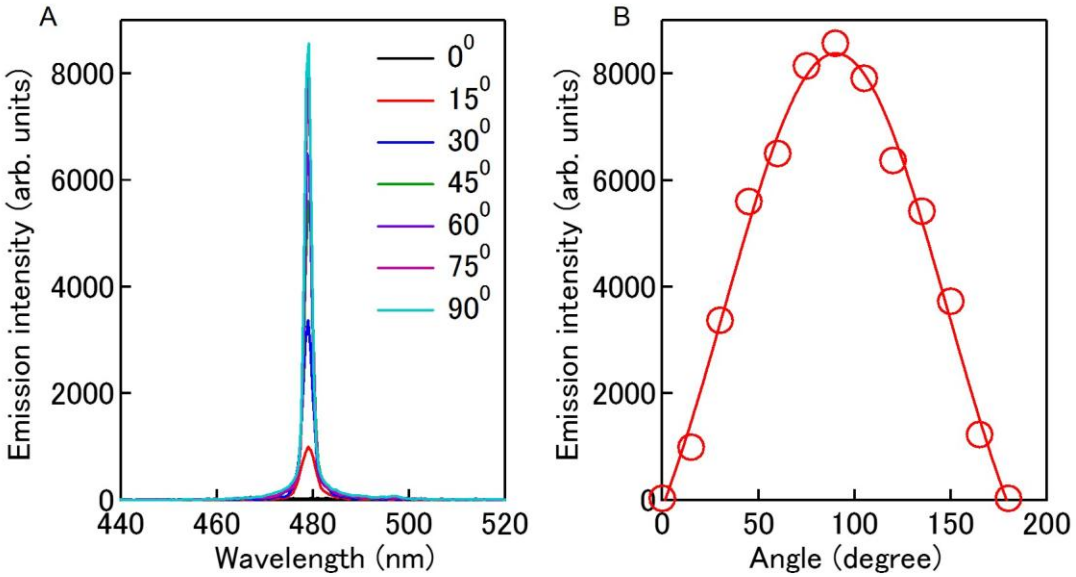

fig. S14. Polarization of DFB laser. (**A**) Emission spectra as a function of the polarization angle and (**B**) emission intensity as a function of the polarization angle. The device was based on a BSBCz:CBP (20:80 wt.%) blend and used a mixed-order DFB grating. The pumping intensity was 200 W cm^{-2} and pump pulse duration was 800 µs. Note that 0° corresponds to the direction parallel to the grooves of the DFB grating.

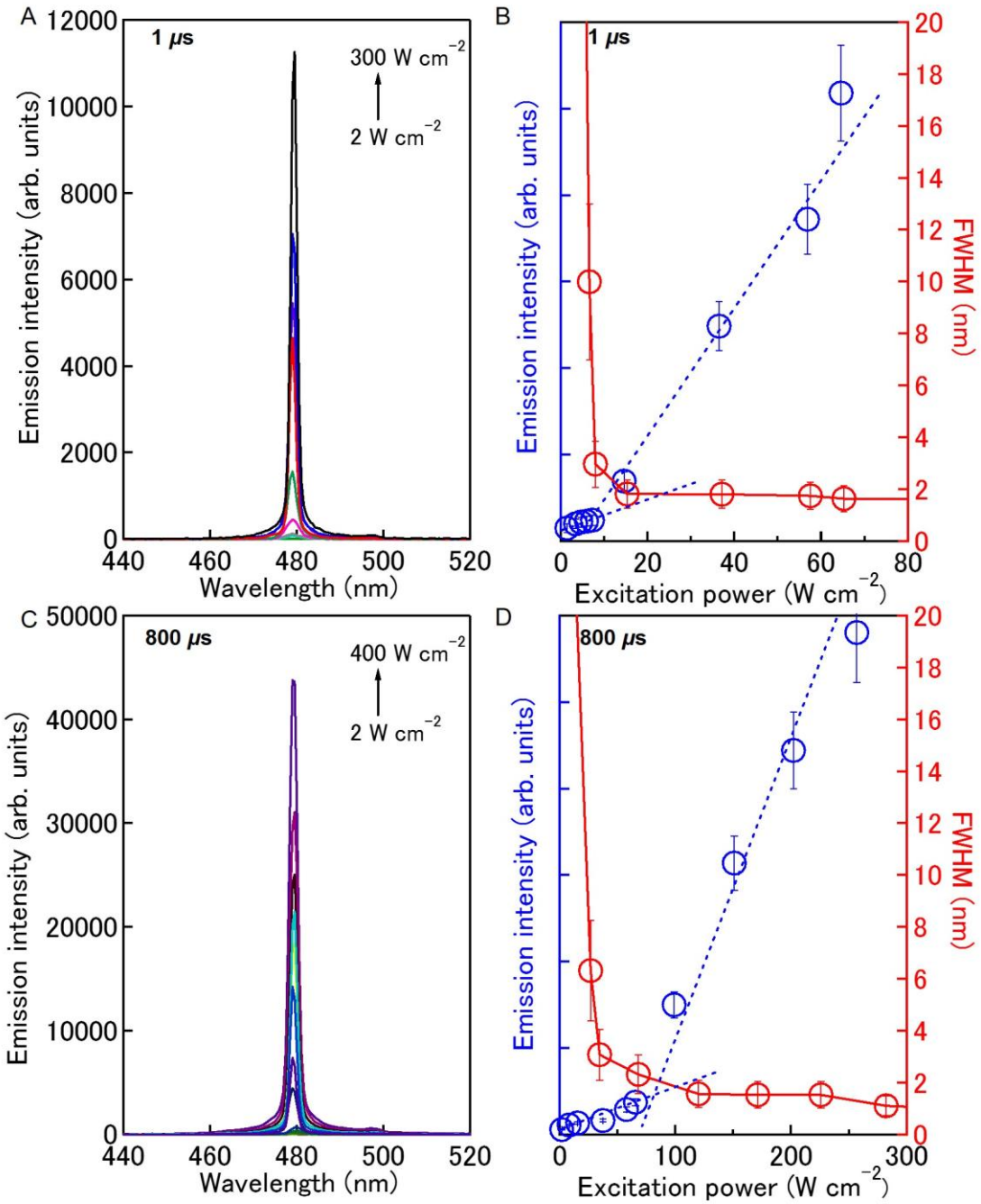

fig. S15. Lasing threshold under long-pulse operation. Emission spectra and laser output intensity and FWHM of an encapsulated mixed-order blend device as a function of the pumping intensities for pulse excitation widths of (**A**, **B**) 1 μs and (**C**, **D**) 800 μs.

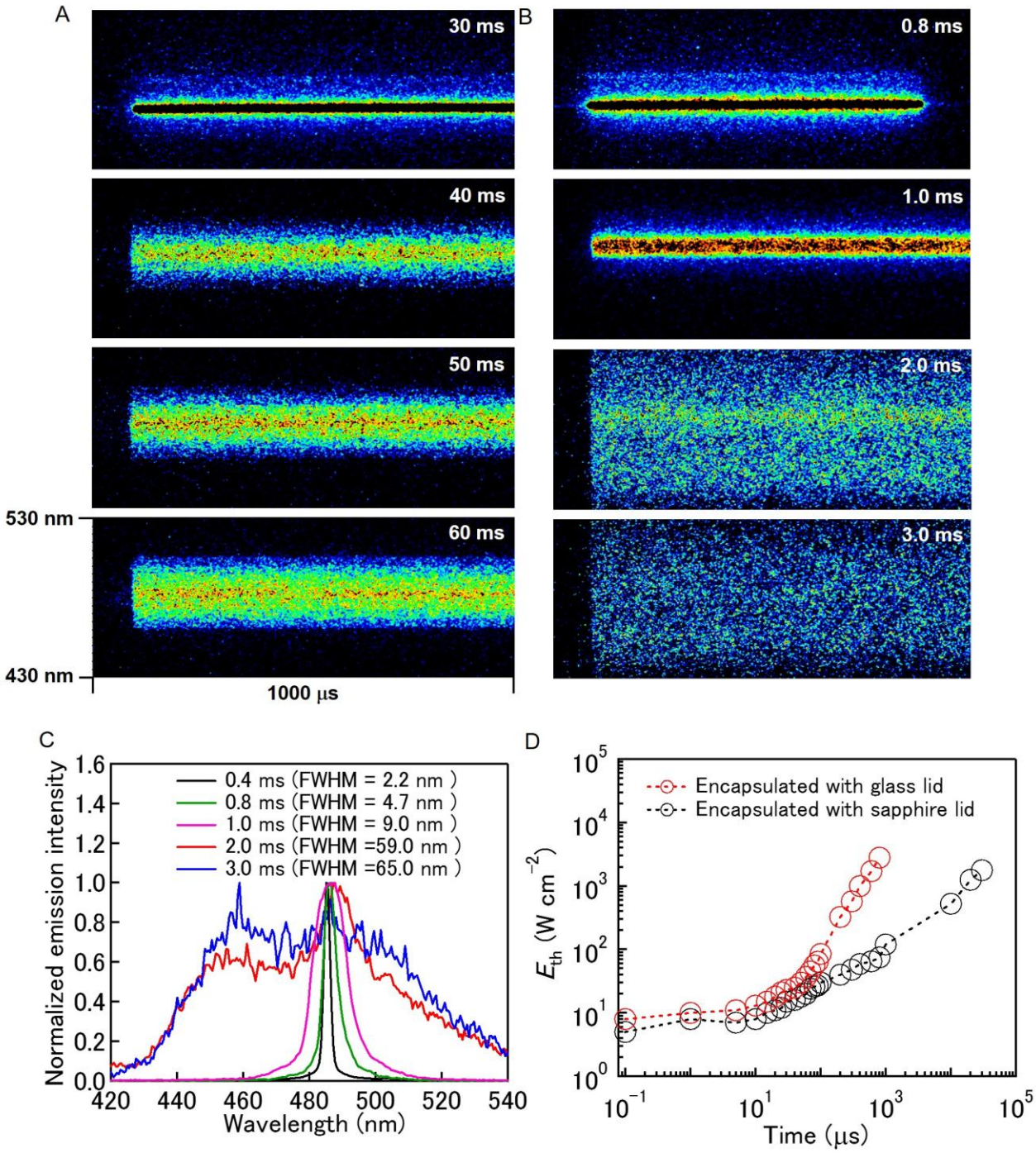

fig. S16. Excitation duration dependence of the lasing threshold. Streak camera images showing laser emission from a mixed-order blend BSBCz:CBP (20:80 wt.%) DFB device encapsulated with a (**A**) sapphire or (**B**) glass lid. (**C**) Emission spectra of the device encapsulated with a glass lid for various pulses widths with a pumping intensity of 2.0 kW cm^{-2}. The emission spectra become broader as the pulse width is lengthened, which can be explained by the significant increase of the lasing threshold with the pulse width. For instance, in the case of the pulse widths of 2 and 3 ms, the device operates below the lasing threshold. (**D**) Lasing thresholds (E_{th}) measured in the BSBCz:CBP (20:80 wt.%) DFB devices encapsulated with

either a sapphire or glass lid as a function of the excitation pulse width. Dotted lines are guidelines for the eye.

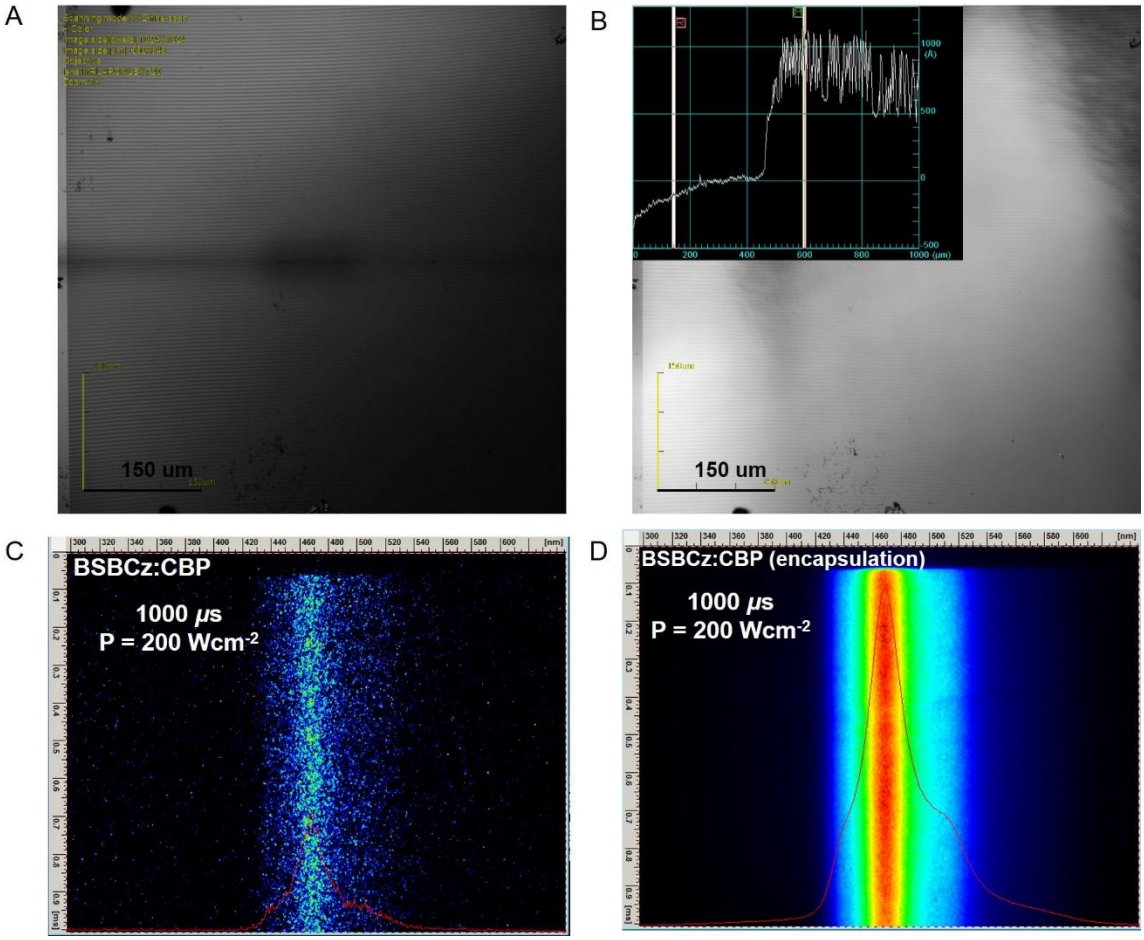

fig. S17. Laser-induced thermal degradation. Laser microscope images of a non-encapsulated blend mixed-order DFB laser (**A**) before and (**B**) after irradiation by 100 excitation pulses with widths of 1 ms. The thickness profile in the inset of (**B**) shows that the organic thin film was ablated during the high intensity CW irradiation. Pumping intensity was 200 W cm^{-2}. The streak camera images in (**C**) and (**D**) show the emission from blend with and without encapsulation under the same irradiation conditions (1 ms pulse width, pumping intensity of 200 W cm^{-2} and integration of the streak camera image over 100 pulses).

section S5. Thermal simulations

Transient 2D heat transfer simulation is performed using COMSOL 5.2a in order to probe the temperature distribution within the device. Figure S18 shows a schematic of the geometry of the laser device. Note that we neglected the grating in this simulation.

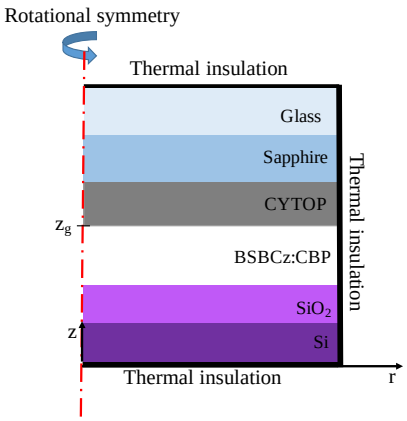

fig. S18. Schematic of the geometry used for thermal simulation.

The governing partial differential equation for temperature distribution is expressed as

$$\rho C_p \frac{\partial T}{\partial t} - k\left[\frac{\partial^2 T}{\partial r^2} + \frac{1}{r}\frac{\partial T}{\partial r} + \frac{\partial^2 T}{\partial z^2}\right] = Q \tag{1}$$

where ρ is the material density, C_p is the specific heat capacity, T in the temperature, t is the time, k is the thermal conductivity and Q is the laser heat source term. The laser pump beam has a Gaussian shape. Because of the circular symmetry of the laser beam, the heat transfer equation is solved in cylindrical coordinate. For a pulsed Gaussian laser beam, the heat source is written as follows (*25*)

$$Q(r,z,t) = \alpha(1-R)\eta_g \exp\big(-\alpha(z_g - z)\big)\frac{2P}{\pi r_0^2}\exp\left(-\frac{2r^2}{r_0^2}\right)H(t) \tag{2}$$

where α is the absorption coefficient, R is the reflection of the pump beam at bottom facet of the device, P is the incident pump power reaching the gain region, r and z are the spatial coordinate, r_0 is the $1/e^2$ radius of the pump laser beam, r=0 is center of the laser beam, z_g is z-coordinate of

the interface between the gain region and the top layers (see fig. S18), $H(t)$ is the rectangular pulse function with a pulse width τ_p, η_g is the fraction of the pump power absorbed in the gain region converted to heat in the absence of laser field (*52*) given by

$$\eta_g = 1 - \phi_{PL}\,\lambda_{pump}/\lambda_{laser} \tag{3}$$

where ϕ_{PL} is the fluorescence quantum yield (ϕ_{PL}(BSBCz:CBP)=86%), λ_{pump} is the pump laser wavelength and λ_{laser} is the extracted laser wavelength. Concerning the boundary conditions, in the radial direction, symmetry boundary conditions are used at the axis of rotation. Thermal insulation boundary conditions are applied at the bottom, top and edge surfaces (air convection is neglected). The radius of the device is set to 2.5 mm. The power density is 2 kW/cm^2. Table S5 presents the thermo-physical and geometrical parameters used in the simulations taken from COMSOL database. For the BSBCz:CBP layer, we chose the same thermal parameters for organic materials as in Ref (*52*).

table S5. Thermophysical and geometrical parameters of the materials.

Layer name	k (W K^{-1} m^1)	C_p (J kg^{-1} K^{-1})	ρ (kg m^{-3})	α (m^{-1}) at 405 nm	D (μm)
Glass	1.4	730	2210	0	717
Sapphire	27	900	3900	0	759
CYTOP	0.12	861	2200	0	2
BSBCz:CBP	0.2	1400	1200	1.55 x 10^6	0.2
SiO_2	1.38	703	2203	0	1
Si	130	700	2329	8.00 x 10^6	333

After absorption of the pump laser energy, the BSBCz layer acts as a heat source. The generated heat is transferred by conduction towards the top and bottom layers.

1.1 Pulse width variation

Figures S19 and S20 show the heating effect at the interface of BSBCz/CYTOP layers after each pump pulse width τ_p of 10, 30 and 40 ms.

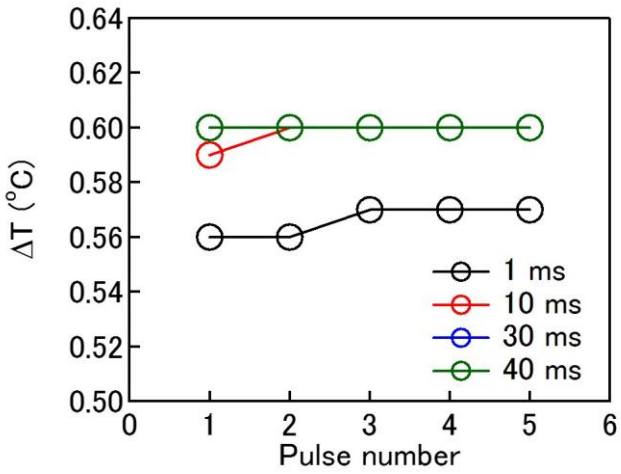

fig. S19. Maximum temperature rise at the end of each pulse.

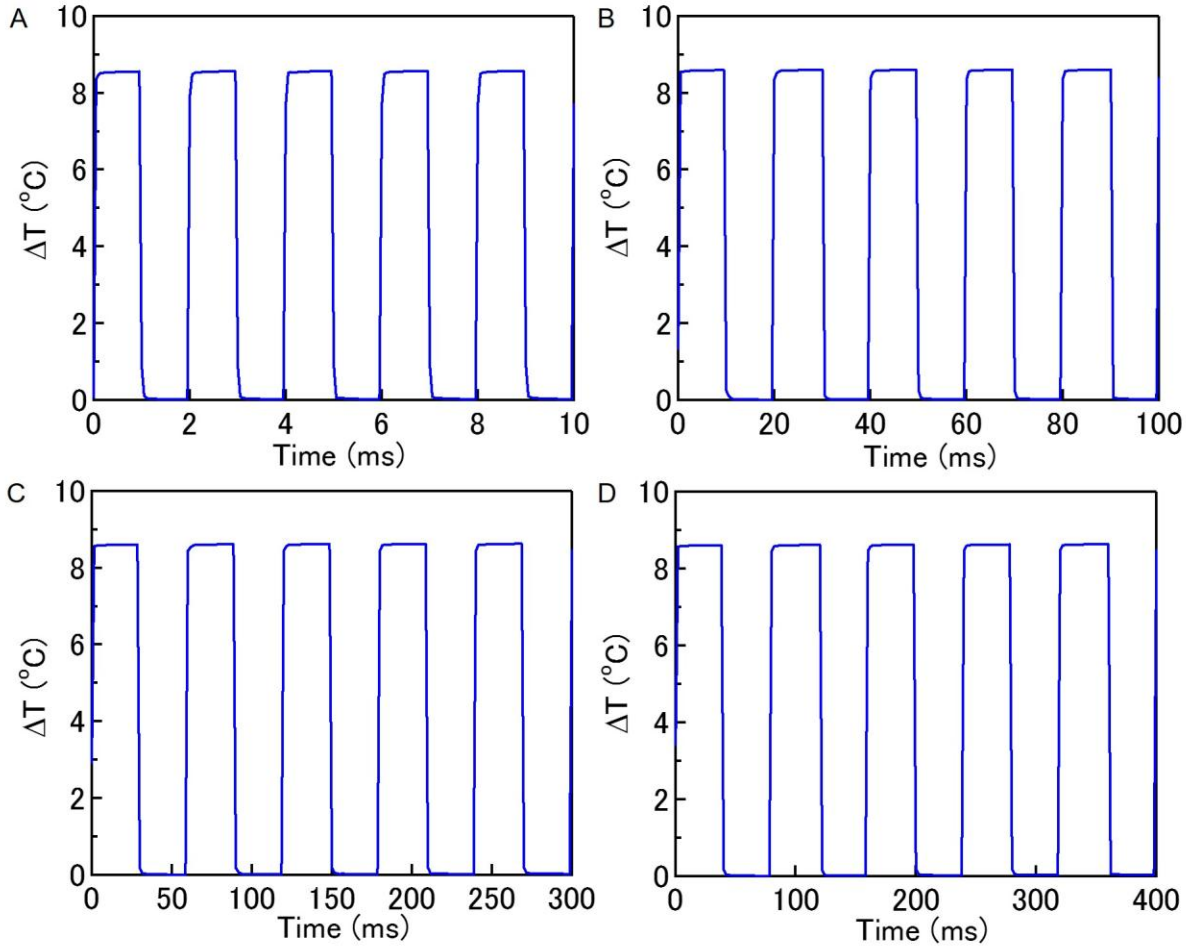

fig. S20. Temperature rise as a function of time with different pulse widths. (**A**) 1 ms, (**B**) 10 ms, (**C**) 30 ms and (**D**) 40 ms.

These simulation results demonstrate that the temperature rise caused by the long pulse pumping irradiation increases with the pulse duration but this effect tends to saturate for pulses longer than 30 ms. It can also be seen from these calculations that the temperature rise is not expected to significantly increase with the number of incident pulses.

1.2 Influence of the encapsulation in the case of a 10ms pulse width

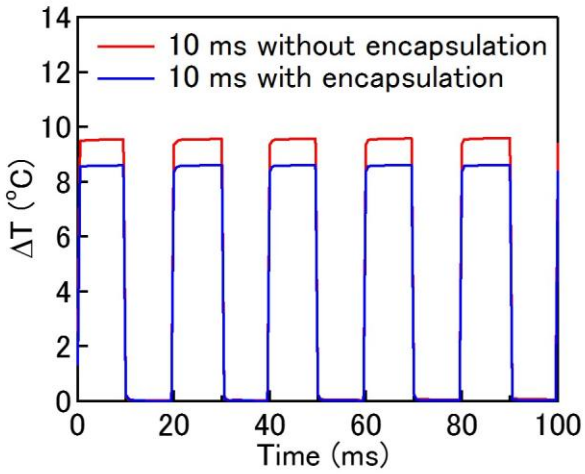

fig. S21. Temperature rise as a function of time for a pulse width of 10 ms in the devices with and without encapsulation.

The simulation results in fig. S21 provide clear evidence of the importance of the encapsulation used in our devices to improve the thermal management in the device operating under long pulse photo-irradiation.

1.3 CYTOP thickness variation

As shown in fig. S22, increasing the CYTOP thickness leads to an increase of temperature in the gain region due to the low thermal conductivity of the CYTOP. While the encapsulation of the DFB laser by CYTOP is found to be critical for improving the performance of the device under long pulse photo-excitation, the poor thermal conduction of CYTOP is clearly a limiting factor and this aspect should be solved in future studies via the selection of a more appropriate encapsulation material in order to demonstrate a real CW organic semiconductor technology.

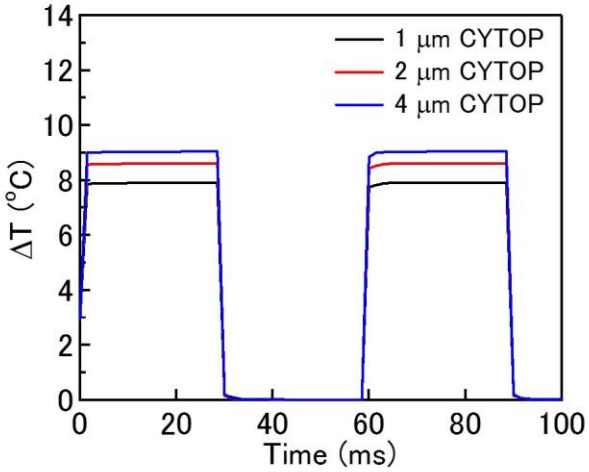

fig. S22. Temperature rise as a function of time or number of pulses of τp = 30 ms in the gain region.